HHS Public Access

Author manuscript

Med Phys. Author manuscript; available in PMC 2019 December 01.

Published in final edited form as:

Med Phys. 2018 December ; 45(12): 5535–5542. doi:10.1002/mp.13223.

An Initial Investigation of Hyperpolarized Gas Tagging Magnetic Resonance Imaging in Evaluating Deformable Image Registration Based Lung Ventilation

Taoran Cui

Department of Radiation Oncology, Rutgers Cancer Institute of New Jersey, New Brunswick, New Jersey, 08901

G. Wilson Miller, **John P. Mugler III**, **Gordon D. Cates Jr**, **Jaime F. Mata**, and **Eduard E. de Lange**

Department of Radiology and Medical Imaging, University of Virginia, Charlottesville, Virginia, 22908

Qijie Huang,

Department of Department of Medical Physics, Memorial Sloan-Kettering Cancer Center, New York, New York 10065

Talissa A. Altes,

Department of Radiology, University of Missouri School of Medicine, Columbia, Missouri, 65212

Fang-Fang Yin, and

Department of Radiation Oncology, Duke University Medical Center, Durham, North Carolina, 27710

Jing Cai[a)]

Department of Health Technology and Informatics, Hong Kong Polytechnic University, Hong Kong

Department of Radiation Oncology, Duke University Medical Center, Durham, North Carolina, 27710

Abstract

Background: Deformable image registration (DIR) based lung ventilation mapping is attractive due to its simplicity, but also challenging due to its susceptibility to errors and uncertainties. In this study we explored the use of 3D Hyperpolarized (HP) gas tagging MRI to evaluate DIR based lung ventilation.

Method and Material: Three healthy volunteers included in this study underwent both 3D HP gas tagging MRI (t-MRI) and 3D proton MRI (p-MRI) using balanced steady state free precession pulse sequence at end of inhalation and end of exhalation. We first obtained the reference displacement vector fields (DVFs) from the t-MRIs by tracking the motion of each tagging grid between the exhalation and the inhalation phases. Then, we determined DIR-based DVFs from the p-MRIs by registering the images at the two phases with two commercial DIR algorithms. Lung

[a)]Please send all correspondence and reprint request to: Jing Cai, Ph.D., Department of Health Technology and Informatics, The Hong Kong Polytechnic University, Phone: (852)-3400 6548, jing.cai@polyu.edu.hk.

ventilations were calculated from both the reference DVFs and the DIR-based DVFs using the Jacobian method and then compared using cross-correlation and mutual information.

Results: The DIR-based lung ventilations calculated using p-MRI varied considerably from the reference lung ventilations based on t-MRI among all three subjects. The lung ventilations generated using Velocity AI were preferable for the better spatial homogeneity and accuracy compared to the ones using MIM, with higher average cross correlation (0.328 v.s. 0.262) and larger average mutual information (0.528 v.s. 0.323).

Conclusion: We demonstrated that different DIR algorithms resulted in different lung ventilation maps due to underlining differences in the DVFs. HP gas tagging MRI provides a unique platform for evaluating DIR-based lung ventilation.

Keywords

DIR; Lung Ventilation; MRI; Hyperpolarized Gas; Lung Cancer

I. INTRODUCTION

Lung ventilation has been used clinically as an important metric to evaluate lung function in patients with chronic obstructive pulmonary disease, asthma or pulmonary embolism. Conventionally, global lung function is measured using spirometry and total lung capacity which provide a global measurement of air flow. Regional ventilation can be measured using alveolar ventilation/perfusion single-photon emission computed tomography (SPECT) scans in nuclear medicine[1–4]. Recently, four dimensional computational tomography (4D-CT) has been widely adapted as an imaging technique to study respiratory motion in radiation therapy of thoracic and abdominal cancers [5]. It has been shown that regional lung ventilation can be estimated based on 4D-CT via deformable image registration (DIR) [6]. When using the DIR-based method of lung ventilation, a displacement vector field (DVF) is first obtained by registering 4D-CT images of two different respiratory phases, typically end-of-inhalation (EOI) phase and end-of-exhalation (EOE) phase. Regional lung ventilation is then calculated as the Jacobian determinate of the DVF [7]. DIR-based lung ventilation mapping has been used for functional-based radiotherapy treatment planning [8–10] and for assessing treatment response of pulmonary function in adaptive radiation therapy for lung cancer [11].

It is critically important yet challenging to evaluate and validate DIR-based lung ventilation, because the method is susceptible to several errors and uncertainties, e.g., image artifacts, inter-technique variability, and variability in DIR algorithms and parameters.[12] There have been only a limited number of studies so far on the validation of DIR-based lung ventilation. For example, lung ventilation based on 4D-CT and DIR has been compared to Xe-CT images in sheep[13], and to SPECT images in humans[14]. It has been shown in these studies that the accuracy of the DIR algorithm significantly affects the ventilation calculation. It was suggested that one should be cautious in selecting the algorithm used for calculation among the various available DIR algorithms [15, 16]. Yamamoto et. al. [17] compared lung ventilations generated using both volumetric and surface-based DIR algorithms. Although both DIR methods resulted in similar deformed images, they produced quite different lung ventilations. These results implied that DIR-based lung ventilation may not reflect true,

physiological ventilation since the DIR algorithms are often designed to match image intensity without considering its physiological plausibility of the results. Studies have also shown that an increased morphological similarity of the aligned data does not always imply increased registration accuracy [18].

Magnetic resonance imaging (MRI) with hyperpolarized (HP) gas (helium-3 [^{3}He] or xenon-129 [^{129}Xe]) has attracted much attention since the first image was acquired in the early 1990s [19]. As the HP gases are inhaled to fill the airway of lung and the alveoli, visualization and measurement of lung ventilation become possible. Recently, HP gas tagging MRI technique has been developed in both 2D [20–22] and 3D [23, 24] for studying pulmonary respiratory dynamics. In this technique, the subject first inhales a dose of HP gas, and the MR pulse sequence creates cube-shaped “islands” of HP gas magnetization distributed uniformly throughout the lungs by saturating the magnetization in uniformly spaced planes. Then, this “tag” pattern is imaged using a 2D or 3D ^{3}He acquisition. Following that, the subject exhales and holds the breath, and the deformed tag pattern is imaged. The positions of each individual tag can then be tracked between two images to create a DVF. HP gas tagging MRI has unique advantages for assessing DIR in the lung: (a) it directly measures regional lung-tissue deformation *in vivo* in human subjects, providing a physiological reference of lung motion; (b) HP gas tagging MR images can embed a large number (~500) of uniformly distributed landmarks within the lungs, allowing for a comprehensive study of the entire lung. On the contrary, current DIR algorithms have difficulties identifying landmarks in in low-featured, peripheral lungs, and therefore are unable to perform accurate deformation registration in these regions. [25, 26] The aim of this work was to investigate the feasibility of using 3D HP gas tagging MRI to assess the physiological accuracy of DIR-based lung ventilation by evaluating two commercial DIR algorithms in three healthy subjects.

II. MATERIALS AND METHODS

II.A. Image acquisition

We developed a hybrid MRI protocol for whole-lung, 3D imaging of two nuclei (protons ^{1}H and either ^{3}He or ^{129}Xe) during a single breath-hold maneuver, using an ultrafast TrueFISP pulse sequence (Siemens Medical Solution; known generically as balanced steady-state free precession or bSSFP). MRI was performed at 1.5 T using a whole-body commercial scanner (Avanto, Siemens Medical Solutions, Malvern, PA). A vest-shaped, proton-blocked RF coil (Clinical MR Solutions, Brookfield, WI) tuned to the appropriate resonance frequency (for either ^{3}He or ^{129}Xe) was used for HP gas imaging. ^{3}He was polarized to ~50% using a homebuilt system, and ^{129}Xe was polarized to ~35% using a prototype commercial system (Xemed LLC, Durham, NH).

The MR image acquisition procedure is illustrated in Figure 1. Conventional proton MR imaging was incorporated directly into our basic HP gas tagging procedure in order to obtain low resolution (Low-R) proton MR images (p-MRI), using the scanner’s integrated body coil, during the same breath hold (and thus at the exact same lung positions) as the HP gas tagging MR images (t-MRI). The requirement to perform tag application plus four 3D image acquisitions (images of two nuclei at both EOI and EOE) within in a single breath-hold

maneuver placed considerable demands on the MR pulse sequence. In particular, we were not able to acquire proton MR images at sufficiently high spatial resolution to perform a meaningful assessment of DIR performance during the same breath hold as the t-MRIs were acquired. We therefore acquired another set of proton MR images with high resolution (High-R), using the scanner's chest and spine array coils, in separate, dedicated breath holds at the same lung positions as the t-MRI acquisitions, using the breath-hold matching procedure described in the next paragraph. The Low-R images were then used to bridge the corresponding t-MRI and High-R p-MRI, as described in the next subsection.

Three healthy subjects (2 female and 1 male, age range 23–31 years) were enrolled in this pilot study under an IRB-approved protocol. Following exhalation to residual volume, each subject inhaled a 1.5 L gas mixture containing between 500 mL and 1L of HP gas, with the balance medical grade nitrogen, and held his or her breath. Next the tag pattern was embedded into the HP gas magnetization, by executing a brief (~1 s) non-imaging pulse sequence that saturated the magnetization in three mutually orthogonal sets of parallel planes as previously described [30–32]. The saturated planes were 14 mm thick and were separated by 12-mm thick sections of undisturbed magnetization, resulting in a 3D tagging grid with isotropic 26 mm tag spacing. The first set of HP gas and Low-R proton images were then acquired, both at 4.5 mm isotropic voxel size, in scan times of 2.2 s and 4.2 s, respectively. Next the subject exhaled into a 0.75 L bag. When the bag was full, the subject held his or her breath and an identical, second set of HP gas and Low-R proton images were acquired. We thereby obtained two complete image sets at two different lung volumes, one at 1.5 L above residual volume (EOI) and the other at 0.75 L above residual volume (EOE), during a single inhalation/exhalation procedure lasting less than 20 s. High resolution (High-R) p-MRI images were acquired at the same EOE and EOI lung positions at 2.5 mm isotropic voxel resolution in separated 17 s scans, using inhalation/exhalation procedures that mimicked the hybrid acquisition protocol. Before the EOI scan, the subject exhaled to residual volume and then inhaled a bag containing 1.5 L of room air. Before the EOE scan, the subject exhaled to residual volume, inhaled a bag containing 1.5 L of room air, and then exhaled into a 0.75 L bag.

II.B. Image Processing

All MR images were imported to the Eclipse treatment planning system (Varian Medical Systems, Palo Alto, CA) for post processing. Since the t-MRI and the Low-R p-MRI were acquired during the same breath-hold, there were no significant spatial shifts between them. To register the t-MRT with the Low-R p-MRI in 3D, we matched the lung surface defined by the outermost tagging grids in the t-MRI with that defined by the boundary between the air and the tissue in the Low-R p-MRI. Although care was taken to ensure that the High-R p-MRI images were acquired at the same lung positions as the t-MRI images, a rigid image registration was performed between each pair of the Low-R and High-R p-MRI images in order to minimize any residual mismatch. Subsequently, the t-MRI was registered to the High-R p-MRI by applying the cascading shifts generated from the two registrations aforementioned. The location of each tagging grid in the t-MRI could therefore be determined with respect to anatomical structures in the same spatial coordinate of High-R p-MRI.

II.C. DVF Generation

Although several methods have been proposed in the literature to track the motion of tagging grids, such as the application of Gabor Filterlter [23] and Matlab-based automatic tracking algorithm [27], they are not designed to and, therefore, are not robust enough to track HP gas tagging grids. In this study, we used a manual tracking method to ensure the accuracies of tagging grid positions and corresponding displacement vectors. The t-MRI images at EOI and at EOE were displayed in Eclipse using the same window/level. The position of each tagging grid was then determined using the spatial coordinates of the grid centroid in the image of each respiratory phase. The difference in the spatial coordinates of each grid centroid was considered as the displacement of that tagging grid. It should be noted that a small percentage (<5%) of the tagging grids either become invisible or too ambiguous to be identified at EOE phase, and were therefore discarded from the analysis. Majority of the tagging grids demonstrated clear boundaries in both respiratory phases and were used to generate lung DVF for the t-MRI images.

DVF for the High-R p-MRI images was generated using DIR to register the images at EOI to that at EOE. Two commercial DIR software, Velocity AI (Varian Medical Systems, Palo Alto, CA) and MIM Maestro (MIM Software, Cleveland, OH), were used in this study. Both DIR software use the intensity-based DIR algorithms and the mutual information as the similarity metrics, but with different transformation algorithms. Velocity AI adapts a spline deformable transformation in which limited number of control points are matched between the target and the moving images, while the deformation of other points are estimated via a B-spline interpolation. In contrast, MIM uses an unlimited number of control points for registration, which, however, requires strict constrains or regulations to find a reasonable solution due to ill conditioning. For both registrations, a cube was selected to include lungs as the region of interest for the registration. The accuracy of the DIR results was reviewed by visually examining the organ overlay and evaluating the difference maps.

II.V. Ventilation Generation and Comparison

For a given lung DVF dataset, the ventilation was calculated using the Jacobian method [28]. In brief, a voxel can be decomposed into six tetrahedrons. Each of tetrahedron is defined by a vertex of the voxel and the other three nearest vertices of the same voxel. The volume of a tetrahedron can be determined given the relative locations of vertices of the tetrahedron. Therefore, once a voxel is meshed into six tetrahedrons, the volume change of the voxel due to a deformation can be conceptually solved by subtracting the total volume of the original tetrahedrons from that of the deformed tetrahedrons. The ventilation of a voxel is therefore defined as the specific volume change of the voxel, which is the volume change divided by the original volume. To account for the different resolutions between the t-MRI and the High-R p-MRI images, we first interpolated the coarser ventilation generated from the t-MRI with a B-spline method, and then compare that to the finer ventilation from the High-R p-MRI.

The differences between the various ventilations, labeled as t-VENT for tagging MRI based ventilation (via manual tracking) and p-VENT for proton MRI based ventilation (via DIR), were quantitatively compared using various metrics, including (1) Mean of ventilation; (2)

Voxel-by-voxel cross correlation of ventilations, where a larger cross correlation would suggest smaller regional difference between the calculated ventilation with the reference t-VENT; and (3) Mutual information of ventilations, where larger mutual information would indicate a stronger dependence between two ventilations, and the mutual information of two independent ones will be zero. The overall study design is shown in Figure 2.

III. RESULTS

III.A. MRI Images

The t-MRI, the Low-R p-MRI, and the High-R p-MRI images of Subject 2 acquired at EOI and EOE are shown in Figure 3. It can be seen that the image are well registered at both respiratory phases, as verified by the matching lung heights (indicted by the yellow dash lines). Furthermore, one can appreciate the high contrast of pulmonary vessels in the High-R p-MRI images using the TrueFISP sequence, which potentially provides ample anatomical information and then improve the credibility of the subsequent DIR. Figure 4 illustrates the alignments of the tagging grids in the t-MRI images to the lung mask defined with the High-R p-MRI images at EOE and EOI. Each colored “bulb” represents a tagging grid at either EOE or EOI, which was generated by the tagging sequence in the t-MRI images. The tagging grids in both two respiratory phases were defined using the same image intensity threshold Therefore, the enlargement of each tagging grid reflected the diffusion of the hyperpolarized gas into the adjacent alveola, and the spatial displacement of each tagging grid can be associated with the respiratory motion of the subject. The majority of tagging grids generated in the t-MRI images at EOI were preserved in those in the t-MRI images at EOE. However, we did notice several grids in the vicinity of lung boundaries disappeared in the images at EOE, especially in the anterior part of the lungs. Moreover, in the inferior part of lung where the motion of the diaphragm was more significant, a few tagging grids might overlap at EOE when the volume of the lung was significantly reduced. Despite of these image artifacts, an average number of 200 tagging grids in each subject were resolved for the following analysis.

III.B. DVFs

Figure 5 shows the comparisons between the DVFs generated from the t-MRI images by tracking the trajectories of the grid centroids (t-DVF) and the DVF generated from the High-R images using Velocity AI ($p\text{-}DVF_{Vel}$). It should be noted that, for illustration purposes, Figure 5 only shows the deformation vectors of the p-DVFs at the tagging grids. The actual resolution of the p-DVF, which was determined by that of the High-R p-MRI images, was much higher than that of the t-DVF, for the number of the resolved tagging grids in a t-MRI image was much less than the number of the voxels in a High-R p-MRI image. Although the overall trends of both DVFs shows that the motion of lung was predominately in the superior-inferior (SI) and the anterior-posterior (AP) directions, the directions and the magnitudes of two DVFs varied noticeably.

The DIRs using both software resulted in reasonably well deformed images, as demonstrated in the difference maps shown in Fig. 6. The High-R p-MRI image at EOI was registered to that at EOE to generate the p-DVF, and the deformed images were obtained by applying the

p-DVF to the High-R p-MRI image at EOI. Given the DIR perfectly registered two images, the deformed image should be identical to the target image. Therefore, the accuracy of the DIR was validated by the small residual errors in the lungs as shown in the difference maps.

III.C. Lung Ventilation

Figure 7 shows the comparisons of three lung ventilations for subject 2. Compared to the t-VENT which is used as a reference, p-VENT generated based on Velocity AI DIR (p-$VENT_{Vel}$) was more homogenous, and therefore more physiologically sound, for ventilation should be a homogenous physiological property throughout the lungs of a healthy subject. On the contrary, p-VENT generated based on MIM DIR (p-$VENT_{MIM}$) was less physiologically sound as several elevated spots of ventilation were observed throughout the lungs. Similar variations were also seen in a quantitative manner in the comparison of the histograms of ventilation (Figure 8) and the voxel-by-voxel joint histogram between the t-VENT and the p-VENT (Figure 9). The histograms of ventilation of the lungs were consistent between the t-t-VENT and the p-$VENT_{Vel}$, with the average ventilations of −0.10±0.19 and −0.08±0.12, respectively. On the other hand, the histogram of p-$VENT_{MIM}$ was skewed to the right with longer tails, resulting in a larger average ventilation of −0.06±0.21. More details were revealed in the voxel-to-voxel comparison in the joint histogram (Fig. 9), that the p-$VENT_{MIM}$ and p-$VENT_{Vel}$ differed significantly from the reference t-VENT with highly scattered distributions. Regardless of the overall differences, p-$VENT_{Vel}$ correlated better with t-VENT than p-$VENT_{MIM}$ with the mutual information of 0.45 v.s. 0.30.

Table 1 summarizes the results of the ventilation comparison for all the subjects. Despite the amplitudes of the respiratory motion varied among the subjects (defined by the diaphragm motion in the SI direction, which ranged from 3.8±0.2 cm to 1.2±0.2 cm), Velocity AI DIR consistently generated more accurate DVFs and ventilations than MIM DIR, as indicated by the smaller errors and the larger cross correlation and mutual information.

IV. DISCUSSION

In this study we investigated a new method based on 3D HP gas tagging MRI to evaluate DIR-based lung ventilation generation. To our best knowledge, this is the first study that compares 3D HP gas tagging MRI and DIR in lung ventilation. As the HP gas tagging MRI provides a direct measurement of lung motion, the derived lung DVF reflects the true lung motion and therefore is an ideal reference for the evaluation of DIR-based lung ventilation. The findings of this study may shed light on the root causes of uncertainties in DIR-based lung ventilation.

Previous studies have demonstrated the potential dosimetric advantages of functional avoidance treatment planning based on lung ventilation in its ability to maximally spare functional lung tissue. Yaremko et al. [10] first proposed to use DIR-based ventilation derived from 4D-CT as the baseline to guide the avoidance in intensity-modulated radiotherapy (IMRT) planning for locally advanced non-small cell lung cancer (NSCLC). Ding et al. [11] investigated the variation of regional ventilation as a response to radiation therapy and further argued that 24 Gy might be the threshold to observe any reduction in lung

ventilation. Vinogradskiy et al. [9] then extended the study of ventilation variation using weekly 4D-CT. Despite these encouraging results, it should be noted that so far no study has correlated DIR-generated lung ventilation with the physiological reference. Besides the weak correlations with SPECT measurement that have been reported [14], Yamamoto et. al. [16] specifically showed that the accuracy of DIR-based ventilation heavily relies on the DIR algorithms. Therefore, with the physiological reference of lung ventilation provided by the HP gas tagging MRI during breathing, we were able to evaluate the lung ventilations based on two commercial DIR algorithms.

Both DIR algorithms used in this study were able to produce reasonable image registrations, partly due to the high contrast of blood vessels and the rich internal features provided by the TrueFISP MR sequence. However, the lung ventilations generated with the two DIR algorithms were different in both magnitude and homogeneity. These variations may be explained by the insufficient registration objectives in those DIR algorithms. The DIR algorithms were designed to achieve best intensity match between target and moving images. The DIR-based DVFs were allowed to vary without enforcing the restrictions posed by the physiological properties of deformed organs, as long as the DVFs minimize the intensity difference between the two images. Although the regularization terms commonly used in the registration were included in the cost function to ensure image smoothness [30, 31] or to maintain physical properties [32, 33], they might not explicitly count for regional lung ventilation. Hence, when using a DIR algorithm to calculate regional lung ventilation, one has to be cautious about whether the intrinsic registration error could jeopardize the ventilation results.

It should be noted that the comparison between two commercial registration software was solely to demonstrate that the accuracy of ventilation calculation is affected by the physiological soundness of the DIR algorithm. As demonstrated, both Velocity AI and MIM resulted in reasonably good registrations with small residual errors, regardless of the discrepancies between their corresponding DIR-based ventilations and the reference t-VENT. Despite that both DIR software have been investigated extensively for a wide range of clinical applications in different clinical setting, studies on their applicability for lung ventilation applications is relatively limited and therefore one should be cautious when using either of them for ventilation mapping.

This study is subject to limitations. Firstly, this study is a preliminary investigation with only two DIR algorithms and three healthy human subjects included. The goal of the study is to demonstrate the feasibility and uniqueness of using the HP gas tagging MRI technique for assessing the physiological soundness of DIR-based lung ventilation mapping. A more comprehensive study with a larger number of subjects and more DIR algorithms is warranted in our future work to evaluate the effectiveness of the HP gas tagging MRI technique for assessing DIR-based lung ventilation. Secondly, it would be more interesting to include HP gas MR ventilation images in this study so that three types of ventilations (gas ventilation, tagging ventilation, and DIR ventilation) can be compared across simultaneously, which would provide more insights into the different methods of lung ventilation. It was unfortunate that the HP gas MR ventilation images were not acquired for the three subjects included in this study. It should be noted that, although related, HP gas

MR ventilation images are fundamentally distinctive from DIR-based ventilation images. The image intensity of a HP gas MR ventilation image is directly proportional to the concentration of the HP gas. Therefore, the intensity variation in a series of HP gas MR ventilation images during a breathing cycle reflects the change of the concentration of the HP gas, which does not necessarily reflect the volume change as defined in DIR-based ventilation method. Hence, it should be cautious when use HP gas MR ventilation image to validate DIR-based ventilation as they are two different quantities.

V. CONCLUSION

In this study we demonstrated a feasible methodology of using HP gas tagging MRI to evaluate DIR-based lung ventilation. Our preliminary results showed that different DIR algorithms resulted in different lung ventilations due to the underline differences in the DVFs. HP gas tagging MRI provides a unique perspective in evaluating DIR-based lung ventilation.

ACKNOWLEDGEMENT

We thank I. C. Ruset and F. W. Hersman of Xemed LLC for providing hyperpolarized xenon-129 for one of our studies. This work is partly supported by funding from NIH grants R21CA195317 and R01HL105586.

REFERENCES

1. Jögi J, Jonson B, Ekberg M, Bajc M, “Ventilation-perfusion SPECT with 99mTc-DTPA versus Technegas: a head-to-head study in obstructive and nonobstructive disease,” Journal of Nuclear Medicine 51, 735–741 (2010). [PubMed: 20395338]
2. Suga K, “Technical and analytical advances in pulmonary ventilation SPECT with xenon-133 gas and Tc-99m-Technegas,” Annals of nuclear medicine 16, 303–310 (2002). [PubMed: 12230089]
3. Burch WM, Sullivan PJ, McLaren CJ, “Technegas-a new ventilation agent for lung scanning.,” Nuclear medicine communications 7, 865–872 (1986). [PubMed: 3033569]
4. Roach PJ, Schembri GP, Bailey DL, “V/Q Scanning Using SPECT and SPECT/CT,” Journal of Nuclear Medicine 54, 1588–1596 (2013). [PubMed: 23907760]
5. Low DA, Nystrom M, Kalinin E, Parikh P, Dempsey JF, Bradley JD, Mutic S, Wahab SH, Islam T, Christensen G, et al., “A method for the reconstruction of four-dimensional synchronized CT scans acquired during free breathing,” Medical physics 30, 1254–1263 (2003). [PubMed: 12852551]
6. Guerrero T, Sanders K, Castillo E, Zhang Y, Bidaut L, Pan T, Komaki R, “Dynamic ventilation imaging from four-dimensional computed tomography,” Physics in medicine and biology 51, 777 (2006). [PubMed: 16467578]
7. Castillo R, Castillo E, Martinez J, Guerrero T, “Ventilation from four-dimensional computed tomography: density versus Jacobian methods,” Physics in medicine and biology 55, 4661 (2010). [PubMed: 20671351]
8. Yamamoto T, Kabus S, Von Berg J, Lorenz C, Keall PJ, “Impact of four-dimensional computed tomography pulmonary ventilation imaging-based functional avoidance for lung cancer radiotherapy,” International Journal of Radiation Oncology* Biology* Physics 79, 279–288 (2011).
9. Vinogradskiy YY, Castillo R, Castillo E, Chandler A, Martel MK, Guerrero T, “Use of weekly 4DCT-based ventilation maps to quantify changes in lung function for patients undergoing radiation therapy,” Medical physics 39, 289–298 (2012). [PubMed: 22225299]
10. Yaremko BP, Guerrero TM, Noyola-Martinez J, Guerra R, Lege DG, Nguyen LT, Balter PA, Cox JD, Komaki R, “Reduction of normal lung irradiation in locally advanced non-small-cell lung cancer patients, using ventilation images for functional avoidance,” International Journal of Radiation Oncology* Biology* Physics 68, 562–571 (2007).

11. Ding K, Bayouth JE, Buatti JM, Christensen GE, Reinhardt JM, “4DCT-based measurement of changes in pulmonary function following a course of radiation therapy,” Medical physics 37, 1261–1272 (2010). [PubMed: 20384264]
12. Sawant A, Yamamoto T, Cai J, “Treatment planning based on lung functional avoidance is not ready for clinical deployment,” Medical physics2018).
13. Reinhardt JM, Ding K, Cao K, Christensen GE, Hoffman EA, Bodas SV, “Registration-based estimates of local lung tissue expansion compared to xenon CT measures of specific ventilation,” Medical image analysis 12, 752–763 (2008). [PubMed: 18501665]
14. Yamamoto T, Kabus S, von Berg J, Lorenz C, Goris ML, Loo BW, Jr, Keall PJ, “Evaluation of four-dimensional (4D) computed tomography (CT) pulmonary ventilation imaging by comparison with single photon emission computed tomography (SPECT) scans for a lung cancer patient.”
15. Kashani R, Hub M, Balter JM, Kessler ML, Dong L, Zhang L, Xing L, Xie Y, Hawkes D, Schnabel JA, et al., “Objective assessment of deformable image registration in radiotherapy: A multi-institution study,” Medical physics 35, 5944–5953 (2008). [PubMed: 19175149]
16. Brock KK, Consortium DRA, et al., “Results of a multi-institution deformable registration accuracy study (MIDRAS),” International Journal of Radiation Oncology* Biology* Physics 76, 583–596 (2010).
17. Yamamoto T, Kabus S, Klinder T, von Berg J, Lorenz C, Loo BW, Jr, Keall PJ, “Four-dimensional computed tomography pulmonary ventilation images vary with deformable image registration algorithms and metrics,” Medical physics 38, 1348–1358 (2011). [PubMed: 21520845]
18. Castillo R, Castillo E, Guerra R, Johnson VE, McPhail T, Garg AK, Guerrero T, “A framework for evaluation of deformable image registration spatial accuracy using large landmark point sets,” Physics in medicine and biology 54, 1849–1870 (2009). [PubMed: 19265208]
19. Albert M, Cates G, Driehuys B, Happer W, Saam B, Springer C, Wishnia A, “Biological magnetic resonance imaging using laser-polarized 129Xe,” 1994).
20. Cai J, Altes T, Miller G, Sheng K, Read P, Mata J, Zhong X, Cates G, De Lange E, Mugler J, et al., “MR grid-tagging using hyperpolarized helium-3 for regional quantitative assessment of pulmonary biomechanics and ventilation,” Magnetic Resonance in Medicine 58, 373–380 (2007). [PubMed: 17654579]
21. Cai J, Miller GW, Altes TA, Read PW, Benedict SH, de Lange EE, Cates GD, Brookeman JR, Mugler JP, Sheng K, “Direct measurement of lung motion using hyperpolarized helium-3 MR tagging,” International Journal of Radiation Oncology* Biology* Physics 68, 650–653 (2007).
22. Cai J, Sheng K, Benedict SH, Read PW, Larner JM, Mugler JP, de Lange EE, Cates GD, Miller GW, “Dynamic MRI of grid-tagged hyperpolarized helium-3 for the assessment of lung motion during breathing,” International Journal of Radiation Oncology* Biology* Physics 75, 276–284 (2009).
23. Tustison NJ, Awate SP, Cai J, Altes TA, Miller GW, de Lange EE, Mugler JP, Gee JC, “Pulmonary kinematics from tagged hyperpolarized helium-3 MRI,” Journal of Magnetic Resonance Imaging 31, 1236–1241 (2010). [PubMed: 20432362]
24. Ding K, Miller W, Cao K, Christensen G, Reinhardt J, Benedict S, Libby B, Sheng K, “Quantification of regional lung ventilation from tagged hyperpolarized helium-3 MRI,” in Biomedical Imaging: From Nano to Macro, 2011 IEEE International Symposium on (2011), pp. 1074–1077.
25. Yeo UJ, Supple JR, Taylor ML, Smith R, Kron T, Franich RD, “Performance of 12 DIR algorithms in low-contrast regions for mass and density conserving deformation,” Medical physics 40, 101701 (2013). [PubMed: 24089891]
26. Liu F, Hu Y, Zhang Q, Kincaid R, Goodman KA, Mageras GS, “Evaluation of deformable image registration and a motion model in CT images with limited features,” Physics in medicine and biology 57, 2539–2554 (2012). [PubMed: 22491010]
27. Cai J, Altes TA, Miller GW, Sheng K, Read PW, Mata JF, Zhong X, Cates GD, de Lange EE, Mugler JP, Brookeman JR, “MR grid-tagging using hyperpolarized helium-3 for regional quantitative assessment of pulmonary biomechanics and ventilation,” Magnetic Resonance in Medicine 58, 373–380 (2007). [PubMed: 17654579]

28. Castillo R, Castillo E, Martinez J, Guerrero T, “Ventilation from four-dimensional computed tomography: density versus Jacobian methods,” Physics in medicine and biology 55, 4661–4685 (2010). [PubMed: 20671351]

29. Segars WP, Lalush DS, Frey EC, Manocha D, King MA, Tsui BM, “Improved Dynamic Cardiac Phantom Based on 4D NURBS and Tagged MRI,” IEEE transactions on nuclear science 56, 2728–2738 (2009). [PubMed: 20711514]

30. Lu W, Chen M-L, Olivera GH, Ruchala KJ, Mackie TR, “Fast free-form deformable registration via calculus of variations,” Physics in Medicine and Biology 49, 3067 (2004). [PubMed: 15357182]

31. Castillo E, Castillo R, Martinez J, Shenoy M, Guerrero T, “Four-dimensional deformable image registration using trajectory modeling,” Physics in medicine and biology 55, 305 (2010). [PubMed: 20009196]

32. Brock KK, Dawson LA, Sharpe MB, Moseley DJ, Jaffray DA, “Feasibility of a novel deformable image registration technique to facilitate classification, targeting, and monitoring of tumor and normal tissue,” International Journal of Radiation Oncology* Biology* Physics 64, 1245–1254 (2006).

33. Brock K, Sharpe M, Dawson L, Kim S, Jaffray D, “Accuracy of finite element model-based multi-organ deformable image registration,” Medical physics 32, 1647–1659 (2005). [PubMed: 16013724]

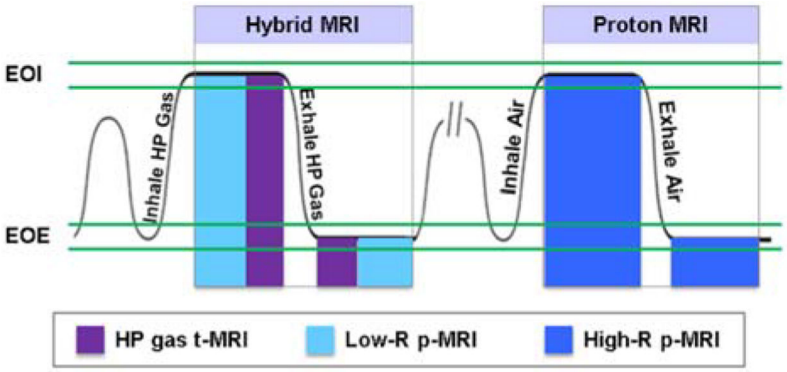

Figure 1.

Schematic diagram of the MR image acquisitions. The subjects inhaled 1.5 L hyperpolarized gas, held breath for a few seconds at EOI, then exhaled 0.75 L of gas and held breath for another few seconds at EOE. A HP gas t-MRI acquisition of 2.2 s duration and a Low-R (4.5 mm isotropic voxel size) p-MRI of acuqisition of 4.2 s duration were acquired during both EOI and EOE periods. High-R (2.5 mm isotropic voxel size) p-MRI acquisitions of 17-s duration was acquired in a seperate breathing cycle with the same 1.5 L inhalation and 0.75 L exhalation volumes.

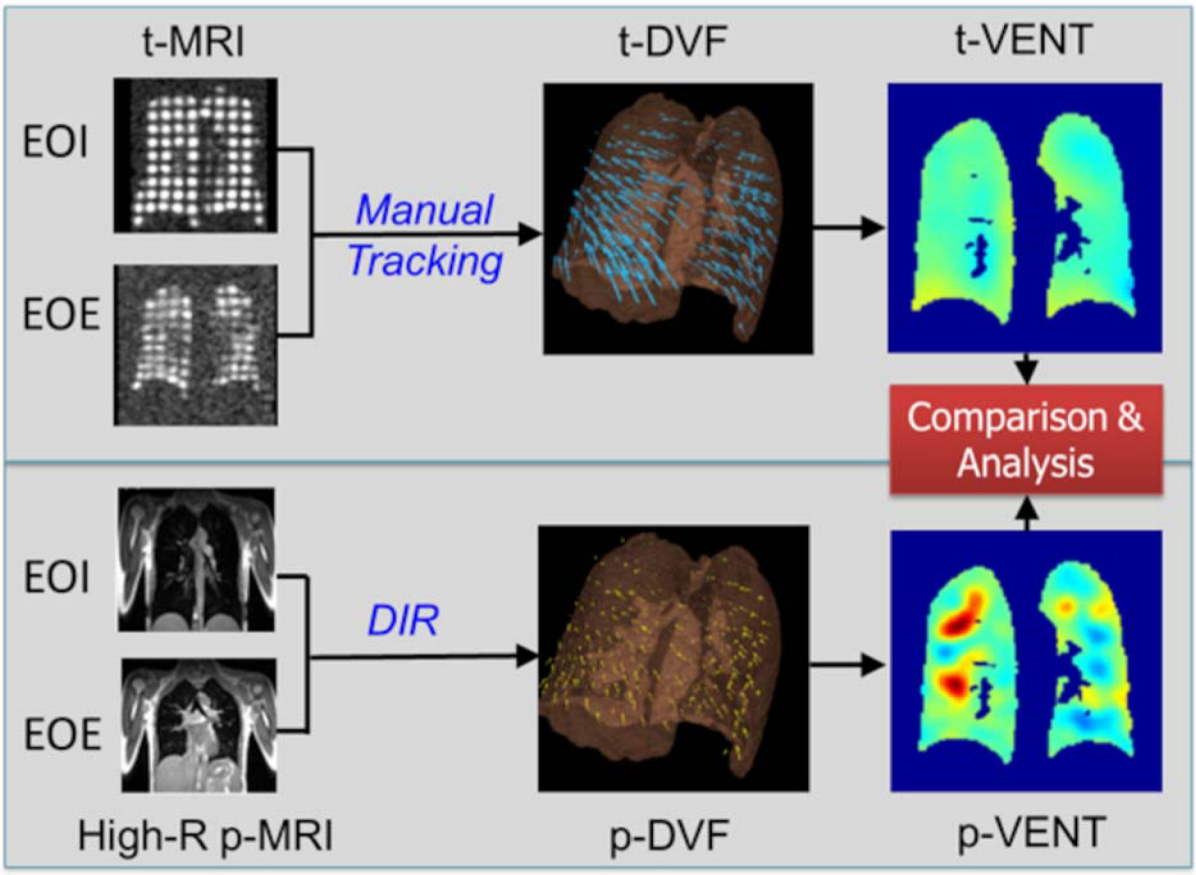

Figure 2.
The overall study design for the evaluation of DIR-based lung ventilation estimation based on HP gas tagging MRI

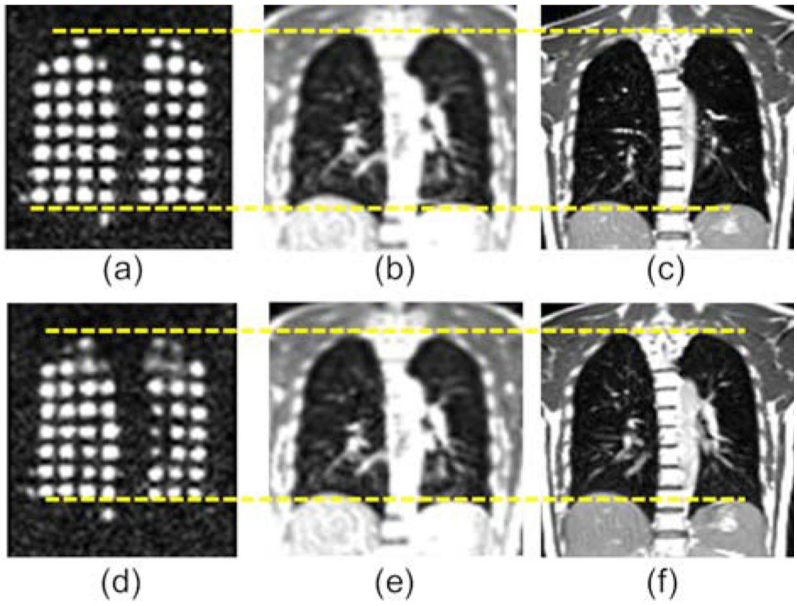

Figure 3:

Representative coronal views of the t-MRI (a,d), the Low-R p-MRI (b,e), and the High-R MRI (c,f) images of Subject 2 inhaling the HP ^{3}He gas at EOI (a,b,c) and EOE (d,e,f), respectively. The images were displayed in the same scale and the same lung heights were measured (indicated by the yellow lines). The FOVs were cropped to only display the lungs.

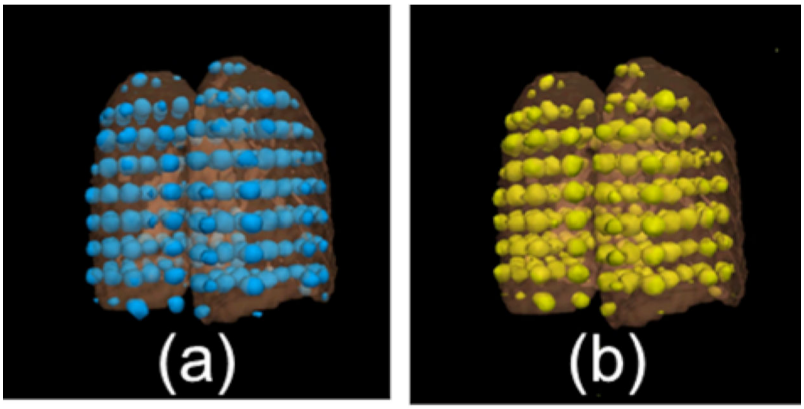

Figure 4:
3D illustrations of the t-MRI images at EOI (a) and EOE (b). The same intensity threshold was used to display the tagging grids in three dimensions.

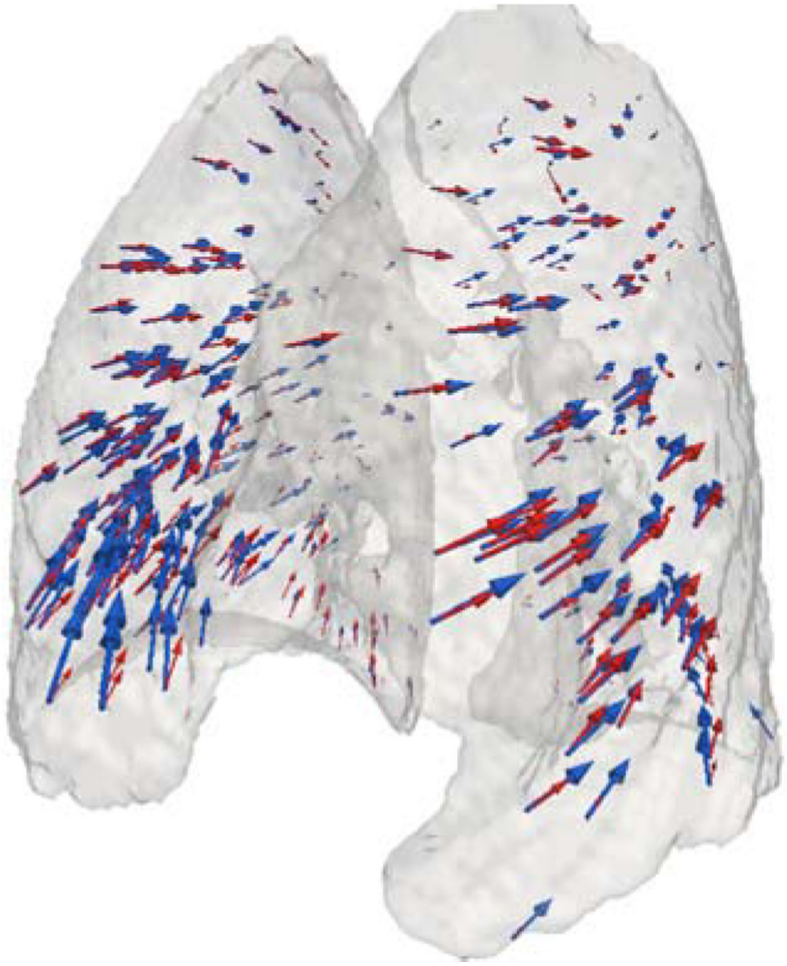

Figure 5:
Comparison of 3D displacement vector fields generated from the t-MRI images with manual tracking (red) and the High-R p-MRI images with Velocity AI (blue) for subject 2.

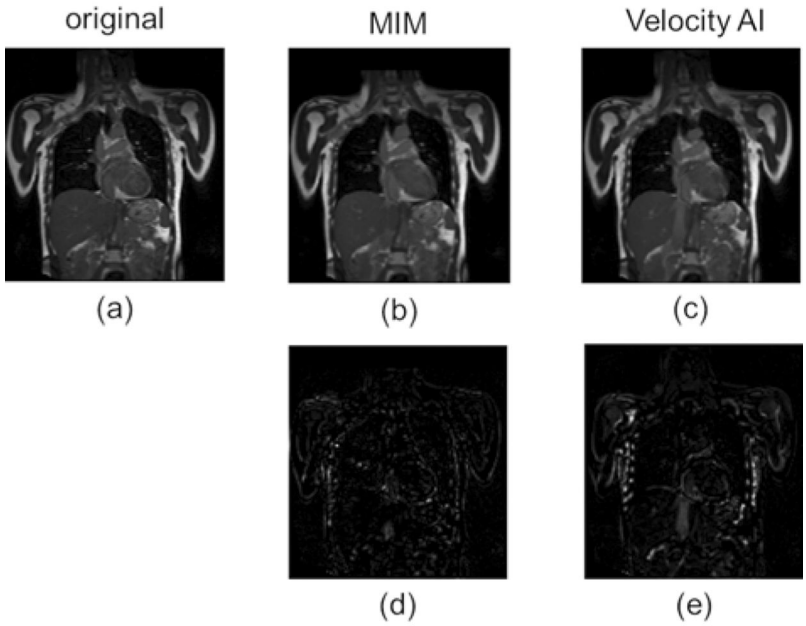

Figure 6:
Demonstrate of the registration results for subject 2. The deformed moving images with MIM (b) and Velocity AI (c) were compared to the target image (a) using the difference images (d,e). The gray scale in the corresponding difference maps represents the residual errors of each registration at a given voxel. The brighter a voxel is, the larger residual error there is in that voxel.

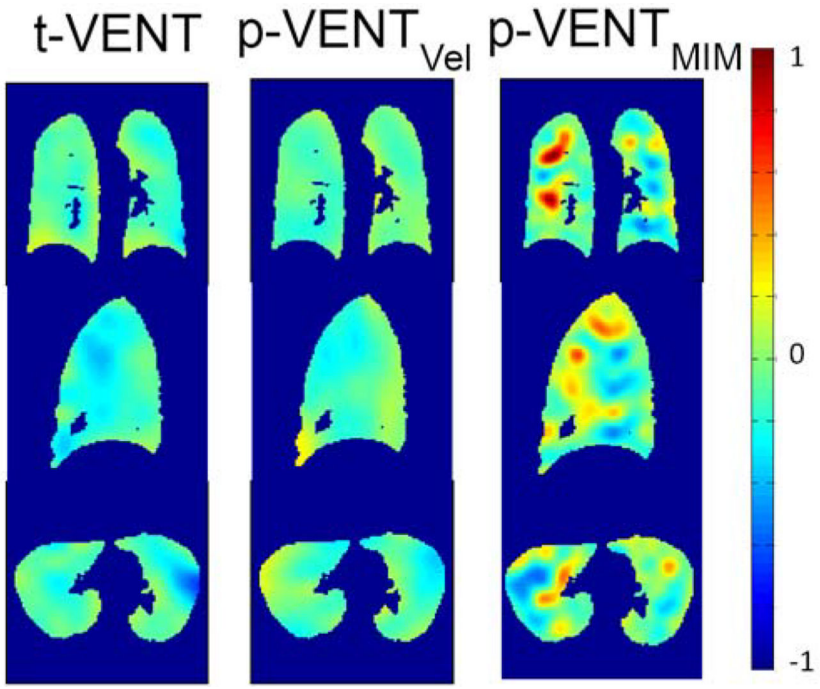

Figure 7:
Comparison of lung ventilations in three orthogonal views for subject 2.

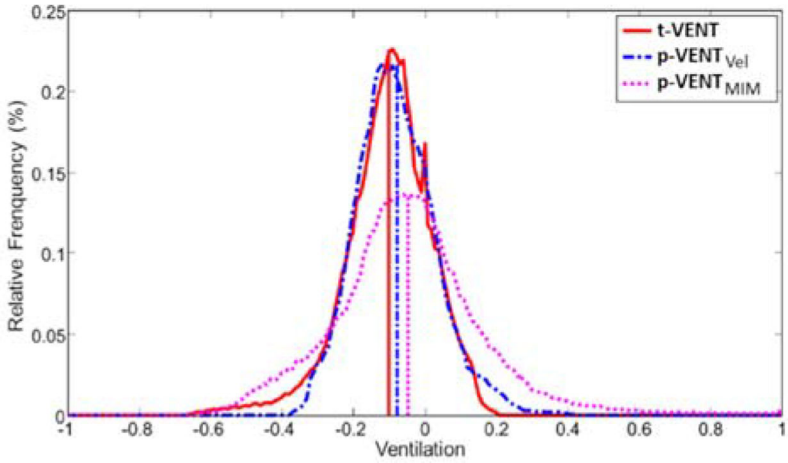

Figure 8:

Distributions of three ventilations of each voxel for subject 2. Red solid line represents the distribution of the reference ventilation, t-VENT, and blue dash line and pink dash lines represent those of two DIR-based results, p-VENT$_{Vel}$ and p-VENT$_{MIM}$, respectively.

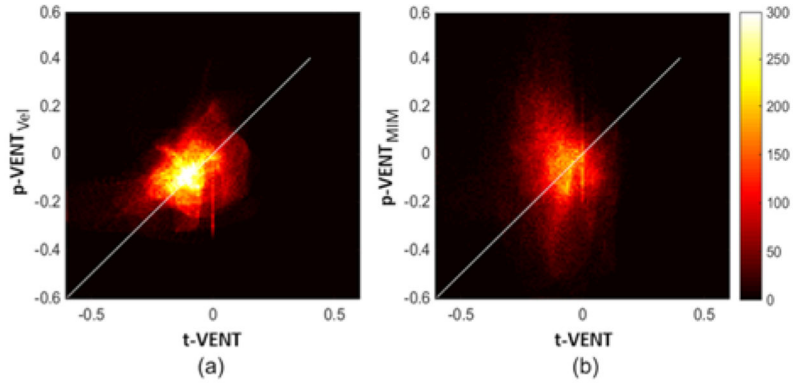

Figure 9:

Joint histograms for t-VENT v.s. p-VENT$_{Vel}$ (a) and for t-VENT v.s. the p-VENT$_{MIM}$ (b) for a representative subject. The horizontal and the vertical axes correspond to the reference ventilation (calculated from t-DVF) and the DIR-based ventilations, respectively. The color scale indicates the number of voxels with the given values of p-VENT and t-VENT. The white line represents the joint histogram of a perfect correlation between p-VENT and t-VENT.

Table 1:

Summary of the ventilation results for three subjects. The diaphragm motion was measured in the superior-inferior direction. Average difference, cross correlation and motion information of p-VENT were compared to the corresponding t-VENT.

Subject	Diaphragm Motion (cm)	Method	Mean	Average Difference	Cross Correlation	Mutual Information
		t-VENT	−0.18±0.29	–	–	–
1	3.8±0.2	p-VENT$_{Vel}$	−0.17±0.21	5.6%	0.3465	0.5880
		p-VENT$_{MIM}$	−0.09±0.17	50.0%	0.1017	0.3665
		t-VENT	−0.10±0.19	–	–	–
2	1.3±0.2	p-VENT$_{Vel}$	−0.08±0.12	20.0%	0.3362	0.4533
		p-VENT$_{MIM}$	−0.06±0.21	40.0%	0.1511	0.3032
		t-VENT	−0.07±0.12	–	–	–
3	1.2 ±0.2	p-VENT$_{Vel}$	−0.08±0.12	14.3%	0.3008	0.5424
		p-VENT$_{MIM}$	−0.04±0.17	42.9%	0.0092	0.3223
		t-VENT	–	–	–	–
Average	2.1±0.3	p-VENT$_{Vel}$	–	13.3%	0.3278	0.5279
		p-VENT$_{MIM}$	–	44.3%	0.0873	0.3307